Inflamed leukocyte-mimetic nanoparticles for molecular imaging of inflammation

Xiaoyue Chen [a], Richard Wong [a], Ildar Khalidov [b], Andrew Y. Wang [c], Jeerapond Leelawattanachai [a], Yi Wang [a,b], Moonsoo M. Jin [a,b,*]

[a] Department of Biomedical Engineering, Cornell University, Ithaca, NY 14853, USA
[b] Department of Radiology, Weill Cornell Medical College, New York, NY 10022, USA
[c] Ocean Nanotech, LLC, Springdale, AR 72764, USA

ARTICLE INFO

ABSTRACT

Dysregulated host inflammatory response causes many diseases, including cardiovascular and neuro-degenerative diseases, cancer, and sepsis. Sensitive detection of the site of inflammation will, therefore, produce a wide-ranging impact on disease diagnosis and treatment. We hypothesized that nanoprobes designed to mimic the molecular interactions occurring between inflamed leukocytes and endothelium may possess selectivity toward diverse host inflammatory responses. To incorporate inflammation-sensitive molecular interactions, super paramagnetic iron oxide nanoparticles were conjugated with integrin lymphocyte function-associated antigen (LFA)-1 I domain, engineered to mimic activated leukocytes in physiology. Whole body optical and magnetic resonance imaging *in vivo* revealed that leukocyte-mimetic nanoparticles localized preferentially to the vasculature within and in the invasive front of the tumor, as well as to the site of acute inflammation. This study explored *in vivo* detection of tumor-associated vasculature with systemically injected inflammation-specific nanoparticles, presenting a possibility of tumor detection by inflamed tumor microenvironment.

© 2011 Elsevier Ltd. All rights reserved.

1. Introduction

Dysregulated inflammatory responses of the host are implicated in the pathogenesis of many human diseases [1]. Acute inflammation from infection can cause sepsis [2], while chronic inflammation, and continual coexistence between acute and chronic inflammation are associated with various neurodegenerative [3] and cardiovascular diseases [4], metabolic disorders [5], and cancer [6,7]. Accordingly, sensitive and early detection of inflammation and site-specific delivery of anti-inflammatory agents will have a wide-ranging impact on the treatment of various inflammation-related diseases. Upon induction of inflammation, a set of adhesion molecules are upregulated in endothelium, with which immune cells interact using counter adhesion molecules such as integrins to adhere to endothelium and to initiate diapedesis. Many existing studies have investigated targeted nanoparticles for the detection and treatment of inflammation employing antibodies or peptides specific to adhesion molecules such as intercellular adhesion molecule (ICAM)-1 [8–10], vascular cell adhesion molecule (VCAM)-1 [11–13], selectins [14], and collagen [15], all of which display distinct spatiotemporal responses to inflammation. Among these molecules, ICAM-1 has caught a particular interest because of its highly inducible and localized expression upon inflammatory signals, serving as a marker for inflammation despite its constitutive low level expression [16,17].

In this study, we developed nanomicelle encapsulating super paramagnetic iron oxide (SPIO) nanoparticles, designed for facile and robust conjugation with targeting moieties and *in vivo* detection by optical imaging and magnetic resonance imaging (MRI). In order to design nanoparticles to mimic the behavior of inflamed leukocytes in their ability to locate to the inflamed site, SPIO nanoparticle was coated with an optimum number of high affinity inserted (I) domain of integrin called lymphocyte function-associated antigen (LFA)-1 [18], a physiological receptor for ICAM-1. Leukocyte-mimetic nanoparticles were examined for detection of ICAM-1 overexpression in tumor cells, tumor vascular microenvironment, and acute inflammation *in vivo*. With our recently developed MRI technique for quantitative mapping of contrast agent [19,20], we explored the possibility of quantitative spatiotemporal mapping of iron oxide distribution *in vivo* using a mouse model of acute inflammation.

2. Materials and methods

2.1. Preparation and characterization of protein coated SPIO nanomicelles

Oleic acid-capped super paramagnetic iron oxide (SPIO) nanocrystals (Ocean Nanotech, LLC) in 5 mg were suspended in 1 ml chloroform with 12 mg

* Corresponding author. Department of Biomedical Engineering, Cornell University, Ithaca, NY 14853, USA.
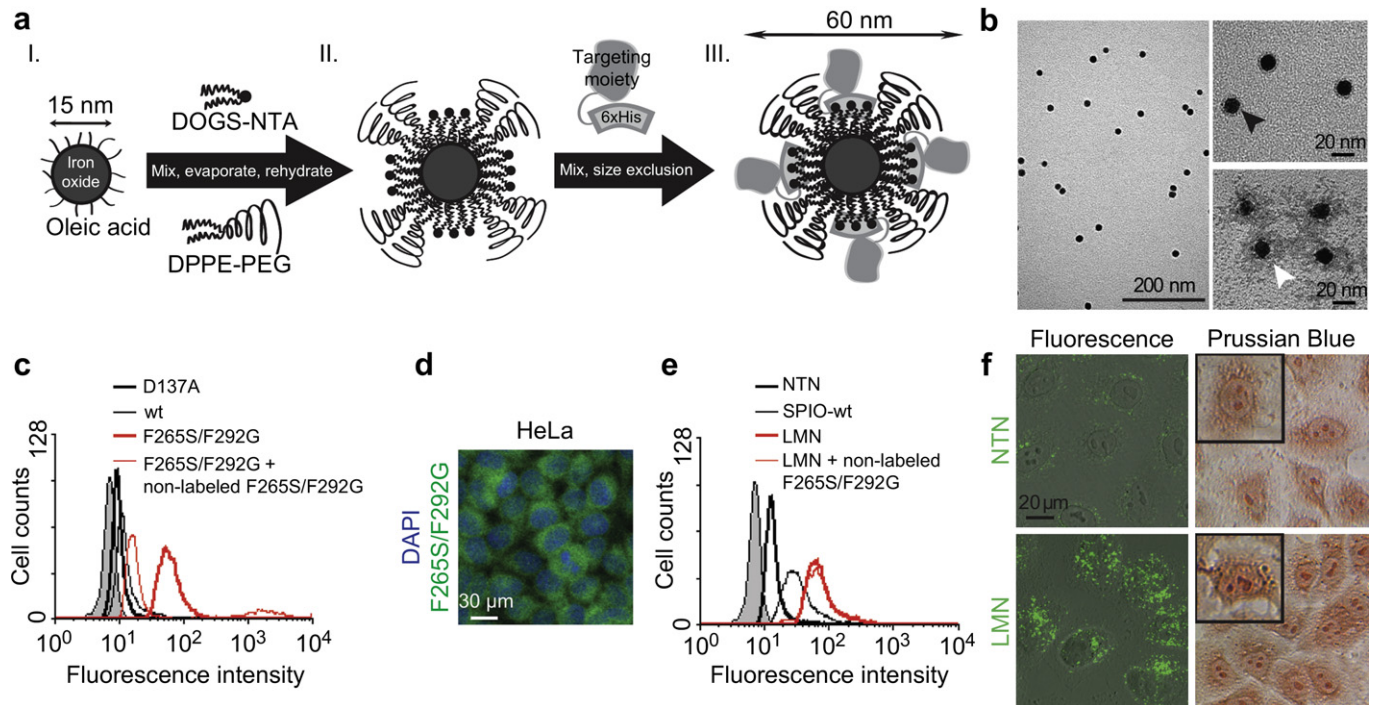E-mail address: mj227@cornell.edu (M.M. Jin).

Fig. 1. Synthesis, characterization, and *in vitro* delivery of leukocyte-mimetic nanoparticles. (a) A schematic diagram of iron oxide nanocrystals encapsulated into a micelle-like layer composed of amphiphilic phospholipid copolymers (stage I–II) and subsequent protein conjugation for molecular targeting (stage III). (b) Uniformly sized, monodispersed SPIO with 15 nm core revealed by TEM. A close up view on top demonstrates a dark halo corresponding to nickel ions (black arrow) chelated by NTA groups surrounding SPIO. On the bottom is the negative staining of protein-conjugated SPIO with proteins and PEG groups darkly stained (white arrow), in contrast to a brighter phospholipid layer. (c) Flow cytometry measurements of HeLa cells stained with different I domains (10 μg/ml) labeled with AF488. Non-stained HeLa cells are shown in grey shaded histograms. In a competition assay, non-labeled I domains were used at 50 μg/ml. (d) Shown in green is immunofluorescence staining of ICAM-1 in HeLa cells using F265S/F292G labeled with AF488. Nuclei staining by DAPI is shown in blue. (e) Flow cytometry measurements of HeLa cells stained with nanoparticles (25 μg/ml of SPIO and 10 μg/ml of I domains) conjugated with different I domains. Non-labeled I domains as a competitor were used at 50 μg/ml (f) ICAM-1 dependent internalization of SPIO into HeLa cells was confirmed with confocal fluorescence microscopy and Perl's Prussian blue staining.

1,2-dipalmitoyl-sn-glycero-3-phosphoethanolamine-N-[methoxy(polyethylene glycol)-2000] (DPPE-PEG) and 3 mg 1,2-dioleoyl-sn-glycero-3-[(N-(5-amino-1-carboxypentyl)-iminodiacetic acid)succinyl] nickel salt (DOGS-NTA) (Avanti Polar Lipids, Inc.). For radiolabeled nanoparticles, 60 μCi of L-α-Dipalmitoyl-Phosphatidylcholine, [Choline-Methyl-3H] (Perkin Elmer) was also added at this step. After 10 min sonication and overnight desiccation, 1 ml of water was added to the residue to form a micelle layer on SPIO. After another 10 min sonication and filtration through 0.22 μm filters (Millipore), optically clear suspension containing SPIO micelles were obtained.

Empty micelles without SPIO in the core were removed by ultracentrifugation. SPIO nanoparticles were purified and resuspended in pH 7.4 phosphate-buffered saline (PBS) by size exclusion S200 column (GE Healthcare). The wild-type (wt), D137A, and F265S/F292G mutants of LFA-1 I domains fused to His tag (6 histidine residues) at the N-terminal were produced as previously described [17]. Conjugation of SPIO with His tagged I domains was obtained by incubation at 4 °C overnight. Free proteins were removed by size exclusion. All fluorescently labeled SPIO nanoparticles were prepared by covalently conjugating Alexa Fluor (AF) succinimidyl esters (Invitrogen)
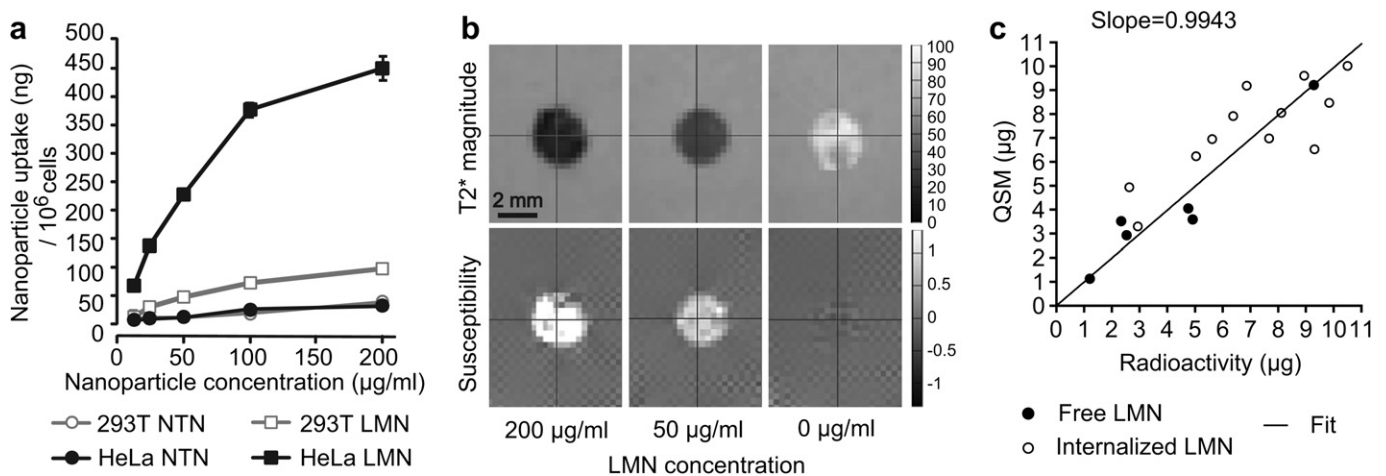

Fig. 2. Quantitative measurement of selective binding of SPIO to ICAM-1 by MRI. (a) The amount of SPIO internalized into HeLa or 293T was measured by radioisotope measurement of ³H-phospholipid incorporated into SPIO nanoparticles. SPIO nanoparticles were coated with either F265S/F292G (LMN) for ICAM-1 targeting or with D137A (NTN) as a control. (b) T2* and susceptibility images of agarose-embedded HeLa cells that were labeled with 200-0 μg/ml of LMN. (c) A comparison of iron mass estimated by QSM technique and radioisotope measurement. Shown are the measurements of agarose-embedded free LMN (closed circles) and LMN internalized into HeLa cells (closed circles).
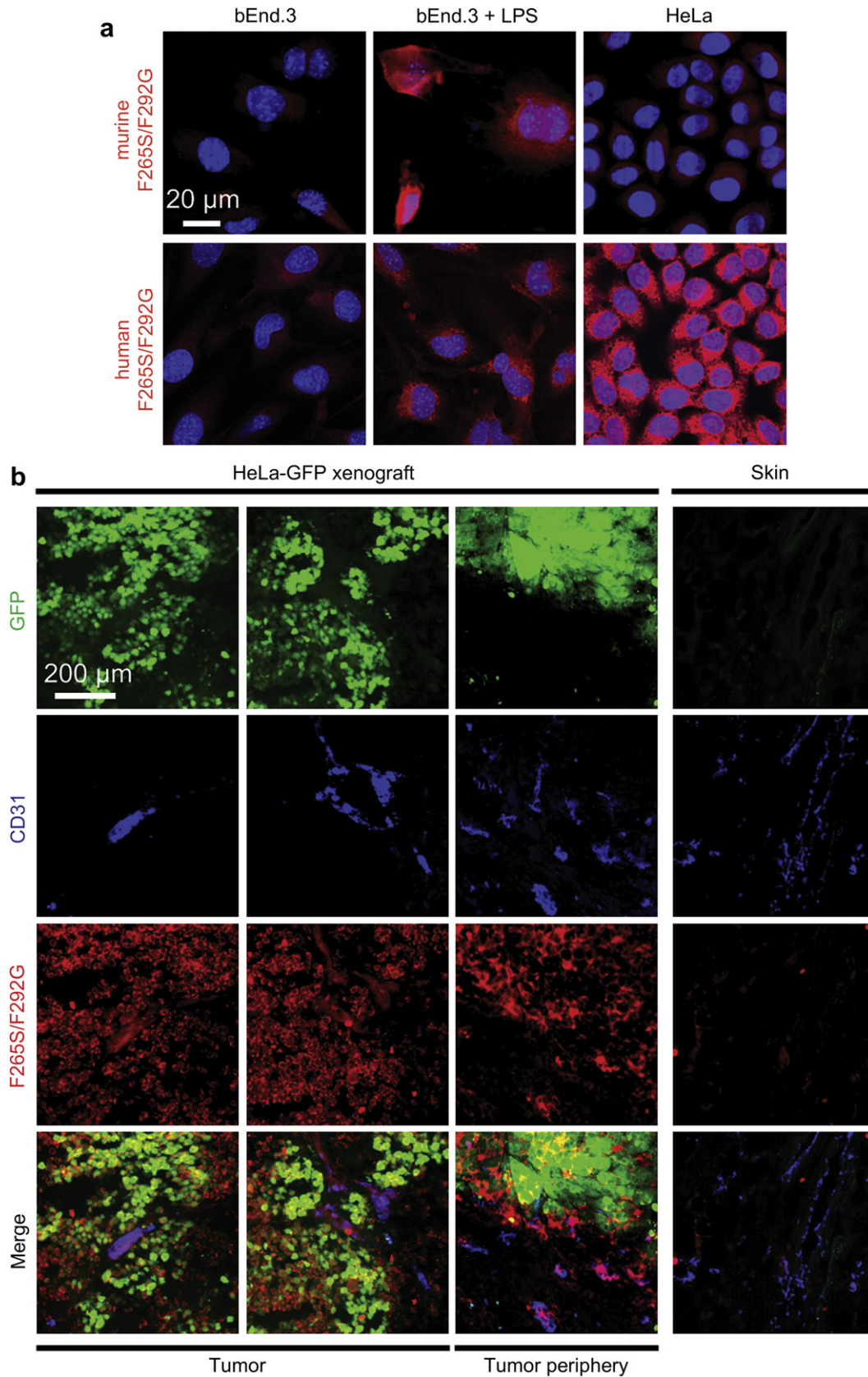
Fig. 3. *Ex vivo* molecular imaging of tumor and tumor-associated vasculature. (a) Confocal fluorescence images of murine b.End3 cells before and after LPS treatment and HeLa cells stained with murine (top) and human (bottom) I domains (F265S/F292G) labeled with AF594. Nuclei staining by DAPI is shown in blue. (b) Immunofluorescence images of GFP-expressing HeLa xenograft tumor tissue costained with F265S/F292G-AF594 and anti-murine CD31 antibodies. Skin tissues from non-tumor bearing mice were used as control. (c) The percentages of endothelium costained with CD31 and F265S/F292G within the tumor, in the periphery (300 μm from the tumor), and in the skin were determined from immunohistology ($n = 6$). (d) Vascularity within the tumor, in the periphery (300 μm from the tumor), and in the skin was quantified using Chalkley's method (25 random points per field of view) ($n = 3$; *$p < 0.05$, **$p < 0.01$).
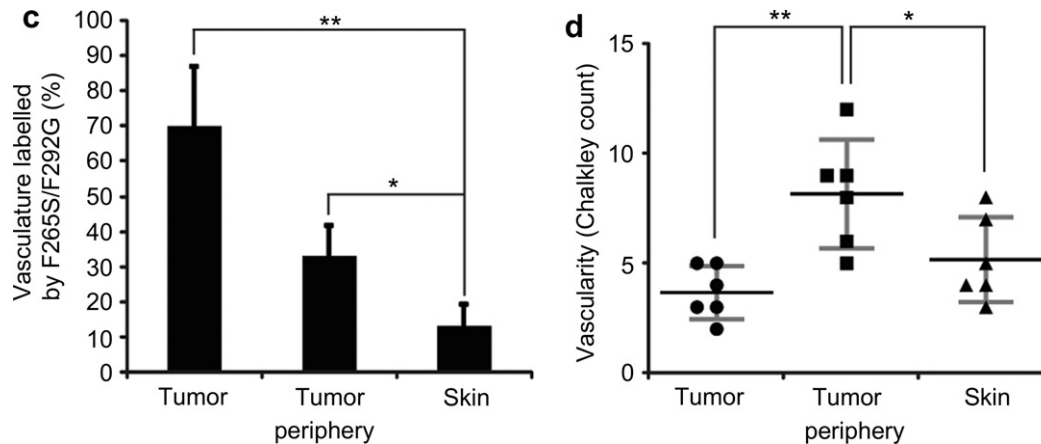
Fig. 3. (continued).

to the I domains. Conjugation of fluorescence dyes to the proteins rather than to phospholipid was chosen due to significant fluorescence quenching between iron oxide and AF-phospholipids. The coating density of proteins on SPIO was determined from the ratio of SPIO amount (OD_{600nm} 1 = 0.42 mg/ml) and the concentration of the proteins bound to SPIO (by Lowry's method). Specific activities of radiolabeled SPIO were measured by scintillation counter (Beckman Coulter LS6500). Dynamic light scattering (DLS, Malvern Instruments) was used to measure the average hydrodynamic size of SPIO after assembly and protein conjugation. Transmission electron microscopy (TEM; FEI Tecnai) images of SPIO were also taken before and after protein conjugation. 1% uranyl acetate was used for protein staining.

2.2. Cell culture

All mammalian cells used in this study were cultured in Advanced Dulbecco's modified Eagle's medium containing 10% (v/v) fetal bovine serum and 2 mM L-glutamine (Invitrogen) at 37 °C in a 5% CO_2 humidified incubator. For induction of inflammation, bEnd.3 (ATCC) cells were treated with 1 μg/ml of LPS (*Escherichia coli.* 026:B6, Sigma) for 12 h. HeLa and 293T cells stably expressing GFP were established using pSMPUW-miR-GFP/Puro Lentiviral Expression Vector system (Cell Biolabs).

2.3. Immunofluorescence flow cytometry

Cells were trypsinized and washed once with the ice-chilled labeling buffer (pH 7.4 PBS, 1% (w/v) BSA, 1 mM $MgCl_2$). 100,000 cells were incubated in 100 μl of the labeling buffer for 30 min on ice with 10 μg/ml of Alexa Fluor labeled proteins or SPIO conjugated with the same amount of proteins. For competition assay, 50 μg/ml of unlabeled proteins were included in the labeling buffer during incubation. Cells were washed twice and resuspended in 300 μl of the labeling buffer and subjected to flow cytometer (Beckman Coulter EPICS XL-MC).

2.4. Microscopy visualization of cell labeling in vitro

For immunofluorescence microscopy detection of protein labeling, cells were plated, washed in pH 7.4 PBS, and fixed with 4% paraformaldehyde for 15 min. After washing three times, cells were incubated with 10 μg/ml of Alexa Fluor labeled proteins in PBS/Triton (pH 7.4 PBS, 0.3% (v/v) Triton X-100, 1 mM $MgCl_2$) at room temperature for 1 h. Cells were rinsed once with pH 7.4 PBS and twice with high salt PBS (pH 7.4 PBS, 0.4 M NaCl, 1 mM $MgCl_2$). 300 nM DAPI (4′,6-diamidino-2-phenylindole, Invitrogen) in PBS was then added and incubated for 10 min for nucleus staining. Stained cells were washed and imaged with a confocal microscope (Zeiss LSM 710). For detection of SPIO labeling, HeLa cells were plated and incubated with 50 μg/ml of SPIO coated with Alexa fluor 488 conjugated proteins in culture media for 2 h at 37 °C. Cells were washed in pH 7.4 PBS, incubated for 1 h in serum-free medium for chasing, and imaged using confocal microscopy (Leica TCS SP2). After fluorescence imaging, cells were then prepared for Perl's Prussian blue staining for iron detection. Labeled cells were fixed with 4% paraformaldehyde, followed by incubation in a freshly prepared solution of 2% potassium ferrocyanide in 2% HCl for 20 min and counterstaining with 1% neutral red.

2.5. Magnetic cell labeling and quantification

Trypsinized cells were incubated for 4 h at 37 °C in the labeling buffer (PBS, 1 mM $MgCl_2$) under constant rotating with different concentrations of radiolabeled SPIO, washed and then fixed in 4% paraformaldehyde. Cells were divided into two conditions, half of which were used for radioactivity measurement using scintillation counter (Beckman Coulter LS6500), while the remaining half for MRI scanning and QSM measurement after imbedding in 100 μl 2% agarose block. MR imaging of the magnetically labeled cells were performed on a 3T MRI scanner (Signa, GE, Milwaukee, WI). A 3D multi-echo gradient sequence was used to sample multiple TEs in one TR. Imaging parameters were as follows: TEs 3.696 ms, 4.196 ms, 5.696 ms, 11.696 ms, 35.696 ms; TR 40 ms; flip angle 30°; matrix size 256 × 64 × 64; voxel size 500 μm³ isotropic. A 3D Fourier transform was applied to the raw k-space data to reconstruct T2* weighted images. QSM was obtained through Multiple Orientation Sampling (COSMOS) technique, as previously described [19].

2.6. Subcutaneous tumor model

$3 × 10^6$ human cervical cancer HeLa cells and human embryonic kidney 293T cells stably expressing GFP mixed in Matrigel (BD) were injected bilaterally into the front lower flank areas of 8-wk-old female nude mice. Mice were used for experiments 16—20 days after injection when tumor size reached about 300 mm³. All animal experiments were conducted in compliance with the regulations defined by the Institutional Laboratory Animal Use and Care Committee of Cornell University.

2.7. Acute LPS-inflammation model

For subcutaneous LPS, 1 mg/ml LPS in 100 μl PBS and 100 μl PBS were injected bilaterally into the lower flank areas of 8-wk-old female BALB/c mice. For systemic LPS, 1 mg/ml LPS in 100 μl PBS were injected into 8-wk-old female BALB/c mice. Prior to imaging hair was removed to reduce background fluorescence.

2.8. Near-IR optical imaging of mice

Animals were anesthetized with isoflurane mixed with oxygen at 5% and maintained at 2% isoflurane during whole body imaging (Olympus, OV100). Mice were administered with SPIO coated with AF750-conjugated proteins in 150 μl PBS via retro-orbital injection. 500 and 100 μg of SPIO were used for tumor imaging and acute inflammation models, respectively. Near-IR images were taken at different time points post-injection of SPIO. Tumor growth was detected by imaging green fluorescence. Image analysis was performed with Matlab R2007a (MathWorks).

2.9. MR imaging of mice with acute inflammation

For subcutaneous LPS model, prior to nanoparticle injection mice were exposed to LPS/PBS for 12 h. At 4 h after injection of SPIO in 150 μl PBS, mice were euthanized by intraperitoneal injection of 2.5% tribromoethanol (20 μl/g), transcardially perfused with PBS, and fixed in paraformaldehyde. Prepared mice were scanned on a 7T scanner (Bruker BioSpin, Biospec 70/30 USR) with 3D FLASH sequence. Imaging parameters were as follows: TEs (echo time) 5 ms, 6 ms, 30 ms, 35 ms; TR (repetition time) 35 ms; excitation pulse angle 15°; matrix size 150 × 150 × 100; voxel size 200 μm³ isotropic; NEX 1. A 3D Fourier transform was applied to the raw k-space data to reconstruct the images [19]. For systemic LPS model, prior to nanoparticle injection mice were exposed to LPS for 12 h. At 1, 8, and 25 h post-injection of SPIO coated with proteins in 150 μl PBS, mice were euthanized likewise. Prepared mice were scanned on a 3T scanner (GE Signa Excite) with 3D multi-echo EFGRE sequence [19]. Imaging parameters were as follows: TEs 3.696 ms, 4.196 ms, 5.696 ms, 11.696 ms, 35.696 ms; TR 40 ms; flip angle 30°; matrix size 256 × 64 × 64; voxel size 500 μm3 isotropic. QSMs were reconstructed using the COSMOS technique, as previously described.

2.10. Histology

Tumor and normal tissues were collected from tumor bearing mice before or at the end of *in vivo* imaging experiments. 10 μm frozen tissue sections were sliced, fixed in paraformaldehyde, and stained with hematoxylin and eosin (H&E) or in Perl's

Prussian blue. Images of the tissue sections were acquired by scanscope (Aperio). For immunofluorescence, antibodies used include rat anti-mouse CD31 (BD, MEC13.3) and goat anti-rat IgG labeled with AF350 (Invitrogen). Six different fields of view containing CD31 staining for each sample were counted using 25 Chalkley's random point method over an area of 0.16 mm^2 for vascularity analysis (Fig. 3d). To quantify the level of staining, three different regions of interest (ROI) with 0.50 mm^2 area were sampled for each condition in immunofluorescence staining (Fig. 3c) and four ROI with 0.04 mm^2 area in each Prussian blue staining (Fig. 4f). Specific colors (blue for endothelium and Prussian blue, red for F265S/F292G) were extracted and intensities were measured using Image-Pro Plus 6.0 (Media Cybernetics) and ImageJ 1.41 (NIH).
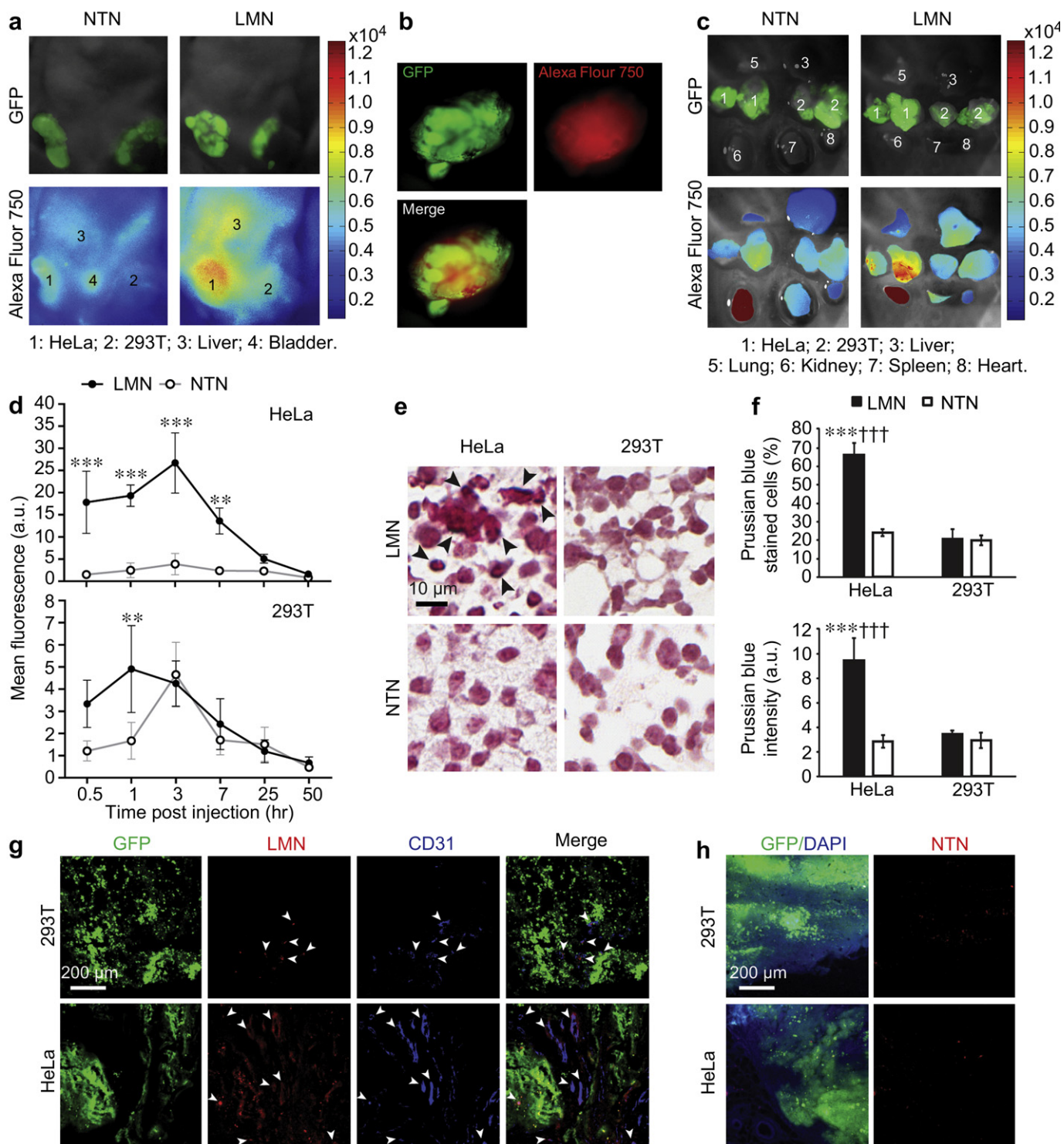

Fig. 4. *In vivo* molecular imaging of tumor and tumor-associated vasculature. *In vivo* (a, b) and *ex vivo* (c) near-IR imaging of mice at 50 h after intravenous injection of NTN vs. LMN. GFP indicates the growth of HeLa ('1') and 293T ('2') tumors. The distribution of nanoparticles into the major organs ('3'-'8') were also examined. (d) Near-IR fluorescence intensities of HeLa and 293T tumors at different time points after intravenous injection of LMN vs. NTN ($n = 4$; **$P < 0.01$, ***$p < 0.001$). (e) Perl's Prussian blue staining of tumor sections collected at 50 h after the injection of LMN vs. NTN. Stained iron is marked with black arrows. (f) Percentage of cells stained in Prussian blue (top) and the intensity of Prussian blue in the field of view (bottom) within tumor sections ($n = 3$; ***$p < 0.001$ between LMN vs. NTN in Hela tumor. $^{†††}p < 0.001$ between HeLa and 293T tumor using LMN). (g) Immunofluorescence imaging of tumors at 4 h post-injection of LMN. Tumor sections were also stained with anti-CD31 antibody for delineating vasculature. LMN localization into the tumor vasculatures was indicated with white arrows. (h) Fluorescence imaging of tumors at 4 h post-injection of NTN.
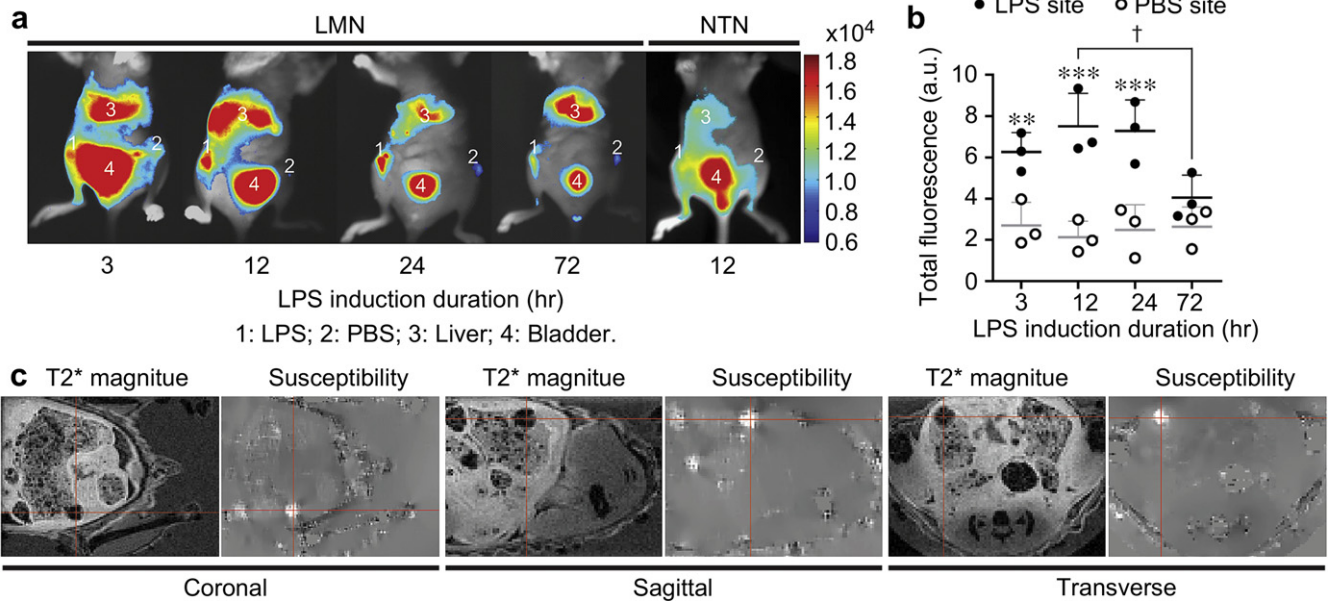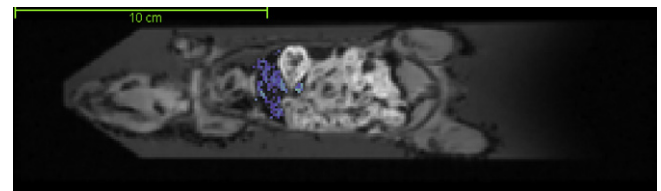
Fig. 5. *In vivo* molecular imaging of subcutaneous acute inflammation using near-IR camera and MRI. (a) *In vivo* near-IR whole body imaging of LMN vs. NTN distribution in mice 1 h after nanoparticle injection. Mice were exposed to LPS ('1') and PBS ('2') for 3, 12, 24, or 72 h at the time of nanoparticle delivery. (b) Fluorescence intensities of LMN at LPS vs. PBS injection sites were shown ($n = 3$; **$p < 0.01$, ***$p < 0.001$ between LPS and PBS site at specific time points; †$p < 0.05$ between 12 h and 72 h at LPS site). (c) T2* magnitude and susceptibility mapping images of nanoparticle distribution in mice at 4 h after nanoparticle injection. Mice were exposed to LPS/PBS for 12 h at the time of nanoparticle injection. Bright spot identified by susceptibility mapping as the accumulation of SPIO was indicated with crosshair.

2.11. Statistical analysis

Data were expressed as mean ± standard deviation of no smaller than triplicates, and analyzed for statistical significance using GraphPad Prism 5 (Graphpad Software). Linear regression was used to examine the correlation between SPIO measurements by radioactivity and QSM (Fig. 2c). One-way ANOVA was used to compare the staining and vascularity levels between different tissues, followed by Tukey's post-hoc test to determine statistical significance (Fig. 3c,d). Two-way ANOVA was used to compare the mean responses of different nanoparticles to different time points or to different tumors, followed by Bonferroni post-hoc test to determine statistical significance (Fig. 4d,f, Fig. 5b, & Fig. 6c,d).

### 2.12. QSM video of mice with systemic LPS injection

The videos corresponding to the data in Fig. 6b are uploaded, providing sagittal, coronal, and axial views of the whole body with the accumulation of LMN or NTN into the liver indicated with the same color scheme as in Fig. 6b. Video S1 (a1.mp4), Video S2 (a8.mp4) and Video S3 (a25.mp4) correspond to the movies of mice at 1, 8, 25 h post-injection of LMN, respectively. Video S4 (i1.mp4), Video S5 (i8.mp4) and Video S6 (i25.mp4) correspond to 1, 8, 25 h post-injection of NTN, respectively.
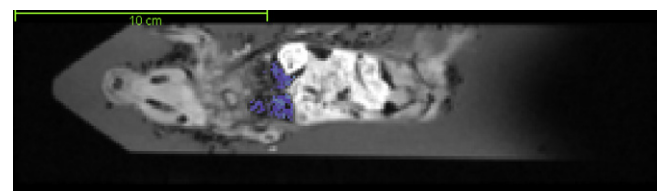

Video S3.
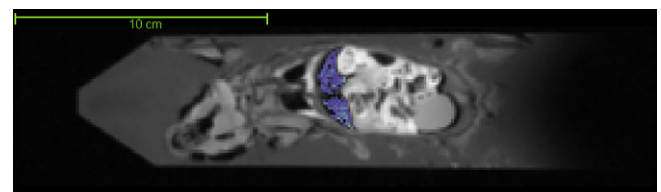
Video S4.
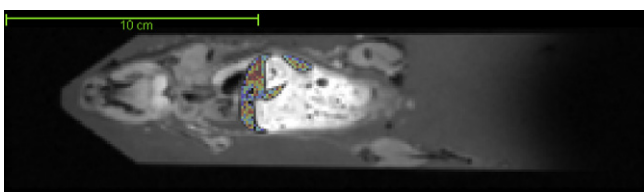
Video S1.

Video S5.
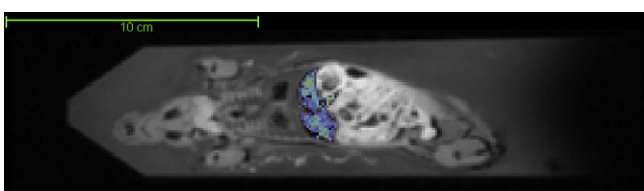
Video S2.
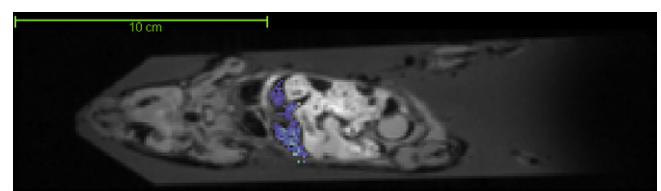
Video S6.
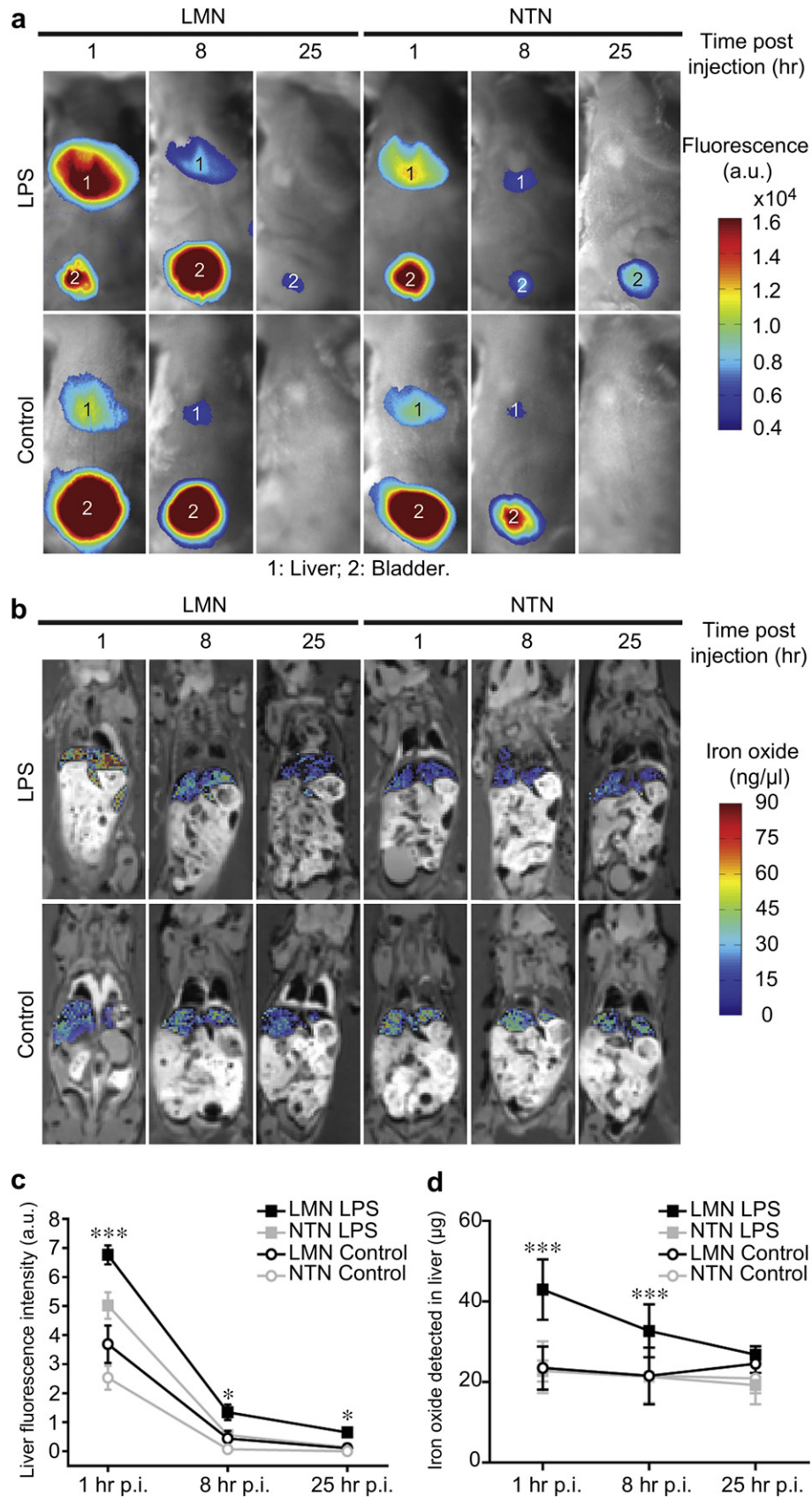
Fig. 6. *In vivo* molecular imaging of systemic acute inflammation using near-IR camera and MRI. *In vivo* near-IR whole body imaging (a) or MRI (b) of LMN vs. NTN distribution in mice at 1, 8, 25 h post-injection of nanoparticles in mice exposed to systemic LPS for 12 h or control mice with no treatment. LMN vs. NTN distributions into the liver were quantified by near-IR optical imaging (c) and MRI (d) ($n = 3$; $*p < 0.05$, $***p < 0.001$ between LMN vs. NTN at specific time points).

3. Results

3.1. Synthesis and characterization of leukocyte-mimetic nanoparticles

Selective binding of SPIO nanoparticles to overexpressed ICAM-1 was conferred by surface coating at an optimal density ($\sim$100 molecular/particle) with the I domain of LFA-1 integrin, engineered for high affinity by mutations of F265S/F292G (denoted as F265S/F292G, $K_D = 6$ nM) [18]. Among physiological ligands for LFA-1 such as ICAMs and junctional adhesion molecule (JAM)-1 [21], ICAM-1 is most important in the setting of leukocyte adhesion to inflamed endothelium due to its highest affinity to LFA-1 [22], being highly inducible over basal low level expression, and localized expression upon inflammatory signals [16,23]. In order to fine-tune coating density of F265S/F292G and present targeting moiety in a most functional orientation, oleic acid-capped SPIO nanocrystals (Ocean Nanotech) were encapsulated with a layer of phospholipid consisting of 80% n-poly(ethylene glycol) phosphatidylethanolamine (DPPE-PEG) and 20% dioleoyl-glycero-succinyl-nitrilotriacetic acid (DOGS-NTA) (Fig. 1a). DOGS-NTA was used for non-covalent conjugation of targeting moieties with His tag in a robust and reproducible manner via high affinity binding to nickel ions chelated by NTA (Ni-NTA) [17,24]. DPPE-PEG was included to maintain solubility, stability, and for its low immunogenicity and non-specific binding to cells and tissues in vivo [25]. Transmission electron microscope (TEM) images revealed monodispersed SPIO nanocyrstals with an outer layer of micelle-like structure (Fig. 1b; dark ring density corresponds to uniformly distributed nickel ions (the black arrow in top right) and diffuse dark density to His-tagged proteins attached to Ni-NTA (the white arrow in bottom right)). Hydrodynamic size of SPIO with or without protein conjugation was measured to be 60 ± 10 nm by dynamic light scattering (DLS), an increase from 15 nm diameter SPIO core mainly due to the addition of phospholipid and PEG.

Prior to detecting ICAM-1 with nanoparticles, we first examined by immunofluorescence flow cytometry (Fig. 1c) and fluorescence microscopy (Fig. 1d) soluble I domain (labeled with Alexa Fluor 488 (AF488), Invitrogen) binding to ICAM-1 expressed in monolayer culture of cervical cancer cells (HeLa). Specific binding to ICAM-1 was detected with the F265S/F292G, which was inhibited by unlabeled F265S/F292G. In contrast, no significant binding was observed with the wt I domain ($K_D = 1.7$ mM) [22] and the I domain containing a mutation of D137A [17], which disrupts the metal-ion dependent adhesion site (MIDAS) and abolishes ICAM-1 binding. The level of nanoparticle binding coated with the I domain variants was overall in good agreement with the soluble I domain binding, which varied in order from highest to lowest, F265S/F292G, wt, and D137A (Fig. 1e). Markedly, specific binding of SPIO conjugated with F265S/F292G (abbreviated as Leukocyte-Mimetic Nanoparticle or 'LMN') was not inhibited by competition with soluble I domain, presumably due to multivalent interaction between nanoparticles and HeLa cells. Enhanced binding due to avidity effect was also observed in the binding of nanoparticle coated with the wt I domain to HeLa, which resulted in greater binding than with the free wt I domain. ICAM-1-mediated binding of LMN but not with the nanoparticles coated with D137A (abbreviated as Non-Targeted Nanoparticle or 'NTN') led to significant cell surface labeling and internalization into the cells, evidenced by fluorescence microscopy and Perl's Prussian blue staining (Fig. 1f).

3.2. Quantitative measurement of selective binding of LMN by MRI

SPIO nanoparticles are being used in clinics as T2* negative contrast agent for MRI. In order to validate SPIO as MRI contrast agent as well as to test the accuracy of our MRI technique for quantitative mapping of SPIO [19], ^{3}H-labeled phospholipid was additionally incorporated into the outer phospholipid layer of SPIO. When HeLa cells were incubated with LMN for 4 h at 37 °C, an increase in concentration led to an increase in cellular uptake of nanoparticles, reaching a plateau at 450 ng/10^6 cells (Fig. 2a). LMN delivery was specific to ICAM-1 expression, evidenced by little accumulation into HeLa with NTN and much lower delivery with LMN into 293T, a cell line with no or little expression of ICAM-1. HeLa cells with known amount of internalized LMN by ^{3}H-radio-isotope decay were then embedded into agarose and scanned with a MRI scanner. As expected, T2* showed a decrease in magnitudes with an increase in the amount of SPIO (Fig. 2b). With quantitative susceptibility mapping (QSM) algorithm was observed a close agreement with $\sim$30% standard deviation from direct radioactivity measurements of free or intracellular SPIO, highlighting the ability of QSM in detecting as low as 1 μg accumulation into 100 μl in volume (Fig. 2c).

3.3. Ex vivo detection of ICAM-1 induction in human tumor xenograft and in inflamed stroma

Not only is ICAM-1 upregulated in several carcinomas compared to respective normal epithelium, implicating active involvement of ICAM-1 in cancer development, its induction has also been observed in tumor vasculature caused by an inflamed network encompassing tumor and tumor microenvironment [26–28]. Previously, we have found that human LFA-1 I domain cross-reacted with murine ICAM-1 [17], which was recapitulated by the staining of ICAM-1 induced in murine brain endothelium (b.End3) after lipopolysaccharide (LPS) treatment (Fig. 3a). When tissue sections of GFP-expressing HeLa xenograft were analyzed for ICAM-1 detection by soluble F265S/F292G labeled with AF594 (Invitrogen), most of the GFP signal was overlapped with red fluorescence (Fig. 3b). Notably, we found that the majority of endothelial cells (PECAM-1 (CD31) positive) within the tumor were also stained by F265S/F292G. In contrast, the level of ICAM-1 induction and colocalization with CD31 staining in the vasculature away from the tumor, such as those in the skin, was far lower, amounting to $\sim$15% compared to 70% and 35% of the vasculature within the tumor and its periphery (defined as a region within 300 μm distance from the edge of tumor), respectively (Fig. 3b–d).

3.4. In vivo detection of ICAM-1 induction in human tumor xenograft and in inflamed stroma

After confirming specific detection of ICAM-1 in ex vivo tumor slice by free F265S/F292G, we then examined if systemically-delivered nanoparticles would accumulate to the tumor and inflamed stroma by ICAM-1 targeting. To validate that nanoparticle localization is ICAM-1 specific and not due to an increased permeability of the tumor vasculature, NTN and ICAM-1 negative 293T cell xenograft were used as controls. The growth of HeLa and 293T xenograft in mice was confirmed by whole body imaging of GFP (Fig. 4a). At 50 h after intravenous injection of nanoparticles, whole body imaging of near-infrared (near-IR) fluorescence (AF750 attached to the I domains) indicated accumulation of LMN into HeLa but much less into 293T xenograft (Fig. 4a,b). Subsequent ex vivo imaging of the tumor and the major organs harvested from the mice further confirmed a greater level of delivery into HeLa xenograft with LMN (Fig. 4c). The signal from the kidney was by far greater than those from other organs both for LMN and NTN, indicating ICAM-1 independent clearance through the kidney (Fig. 4c). Interestingly, higher fluorescence was also detected in the liver with LMN, presumably caused by persistent, low level

inflammation in the liver. Whole body imaging of nanoparticles localized to HeLa and 293T xenograft over the time course of 30 min–50 h post-injection showed that the peak accumulation occurred at 1–3 h post-injection, followed by a gradual decrease over 3 days and a complete clearance by 7 days (Fig. 4d). The presence of LMN into HeLa was also confirmed by direct staining of iron with Prussian blue (Fig. 4e,f). To map the distribution of LMN by fluorescence microscopy, SPIO nanoparticles conjugated with AF594-labeled I domains were intravenously injected into the mice with HeLa/293T xenograft. When the xenograft tissue was examined 4 h after nanoparticle injection, specific accumulation of LMN into HeLa tumor was observed, judging from colocalization between GFP expression in HeLa and AF594 fluorescence (Fig. 4g,h). Importantly, consistent with the detection of ICAM-1 in the tumor vasculature by direct staining of the tissue (Fig. 3b), a high percentage of CD31 positive cells in HeLa as well as in 293T xenografts were also targeted by LMN. The localization of ICAM-1 specific nanoparticles within the tumor-associated vasculature, therefore, was likely responsible for higher signals detected within 293T xenograft at earlier time points (Fig. 4d), despite the fact that 293T itself exhibited almost no binding of LMN (Fig. 4e,f). This finding highlights a potential use of LMN for detection of tumor growth by their accumulation into inflamed tumor vasculature, irrespective of the type of tumor surface antigen.

3.5. In vivo detection of temporal dynamics of inflammation by optical imaging and MRI

In order to further confirm that our leukocyte-mimetic nano-particles sensitively detect the induction of ICAM-1 not only due to an inflammatory milieu in the tumor but also by acutely induced inflammation, we imaged mice after subcutaneous (Fig. 5) or intravenous injection of LPS (Fig. 6). Temporal mapping of nano-particle distribution demonstrated a greater localization of LMN into the LPS injection site over PBS injection site as a control, peaking at 12 h post-injection of LPS and gradually decaying over 72 h (Fig. 5a,b). Higher accumulation into the liver was also observed with LMN, attributed to the inflammatory response induced by the leakage of locally injected LPS into circulation. We also observed a rapid increase in fluorescence in the bladder, irre-spective of targeting moieties, attributed to renal clearance of some fraction of proteins dissociated from nanoparticles. Interestingly, NTN accumulated more into the LPS site than into the PBS site, presumably due to non-specific phagocytosis of nanoparticles by immune cells. Selected mice treated with systemic delivery of 100 μg LMN were then subjected to MRI after whole body optical imaging to demonstrate that our nanoparticles could be used for quantitative detection of inflammation by a clinically relevant imaging technique (Fig. 5c). T2* magnitude images identified the presence of LMN in the LPS injection site as darkness, which could be confused with other dark regions. QSM revealed the accumu-lation of ∼0.3 μg of iron oxide (corresponding to detection of less than 1% of injected dose) into the LPS injection site, colocalized with the site identified by near-IR imaging (Fig. 5a).

In response to systemic inflammation caused by intravenous injection of LPS for 12 h prior to nanoparticle (∼200 μg) injection, optical mapping of nanoparticle distribution demonstrated greater localization of LMN in the liver compared to that of NTN in mice (Fig. 6a,c), peaking at 1hr post-injection of nanoparticles and subsequently diminishing at later time points. The level of delivery overall was higher with LPS even with NTN, indicating some of nanoparticles accumulated into the liver was caused by ICAM-1 independent phagocytosis. After optical imaging, mice were transcardially perfused with PBS for MRI, which would have removed nanoparticles retained in the blood pool in the liver.

Temporal mapping of SPIO distribution using MRI QSM measured about 20% of the total dose of LMN was specifically uptaken by the liver 1 h post-injection due to LPS-induced inflammation (Fig. 6b,d and supplementary videos). QSM quantification also demonstrated a similarly greater localization of LMN into the liver under acute inflammation at different time points, exhibiting qualitative agreement with the temporal mapping using optical imaging (Fig. 6b,d). Discrepancy between optical intensity and QSM was unavoidable as MRI was performed after perfusion of the mice as well as due to the different kinetics of degradation for fluorescence dye (AF750) and SPIO.

Supplementary video related to this article can be found at doi:10.1016/j.biomaterials.2011.06.030.

4. Discussion

Sensitive detection of inflammation will be of high significance for diagnosis of diseases caused directly by host inflammatory response such as sepsis, allograft rejection, lupus, as well as those that are influenced by inflammation such as cardiovascular disease and cancer. In this study, we designed MRI-compatible SPIO nanoparticles, and demonstrated a successful detection of consti-tutive expression of ICAM-1 in tumor, as well as ICAM-1 induction in tumor-associated vasculature, where tumor growth and angio-genesis are active. Prior approaches to inflammation detection have been largely based on antibodies that are against cell adhesion molecules such as ICAM-1 and VCAM-1 [8–13,29], lacking in the ability to fine-tune affinity and avidity of targeting moieties on nanoparticles that are critical to inflammation-specific targeting. From our previous in vitro studies [17,24], we have demonstrated specific localization into inflamed but not to resting endothelium and immune cells of nanoparticle (50–100 nm in diameter) coated with integrin LFA-1 I domain engineered for high affinity to ICAM-1. Furthermore, combining recently developed quantitative suscep-tibility mapping technique, we quantified sub-microgram quantity of iron oxide accumulated in both ICAM-1-expressing cell phantom in vitro and acute inflammation induced by LPS in vivo, corre-sponding to less than 1% of injected dose.

Despite the fact that ICAM-1 is basally expressed in all endo-thelium [16,23] and therefore the notion that ICAM-1 may not be a suitable target for inflammation, our studies emphasize selective delivery by targeting molecules that are induced greatly under inflammation [30,31]. Nanoparticles of ∼100 nm will experience hydrodynamic force generated by the blood flow [32,33], such that there should be sufficient simultaneous molecular interactions with the cells for nanoparticles to remain on cell surface. The number of minimum molecular interactions required for stable adhesion of nanoparticles will also depend on the adhesion strength of each interaction. Therefore, specificity toward high ICAM-1 site will be influenced by the affinity of molecular interaction and the valency between nanoparticles and target cells, where the design of nano-particles to permit tunable affinity and avidity of physiological interaction is of significant advantage. Our nanoparticles to a great extent mimic the behavior of activated leukocytes, which would adhere much better to inflamed endothelium.

Increasing number of studies have begun to focus on the crosstalk between the immune activation of vascular niche, angiogenesis, and tumor progression [34,35]. Upregulated levels of ICAM-1 in tumor have been linked to two different contexts, one serving as a marker for the recruitment of effector immune cells and tumor killing [36], while it was also observed in malignant and metastatic tumors with poor prognosis [37]. Seemingly contra-dicting roles of ICAM-1 may be due to the complexity of inflam-mation in various phases of tumor development, which can be better examined by in vivo imaging tools. Our nanoparticles did

indeed show the localization into the tumor vasculature, while their localization into the vasculature elsewhere was non-detectable. With human tumor xenograft model, we observed that the majority of tumor mass was comprised of tumor cells with poor vascularity present therein. Higher vascularity was found in the periphery of the tumor, often called the invasive tumor front, where ICAM-1 overexpression associated with higher immune activity has also been reported in many carcinoma cases [27,38–41]. Notably, we have demonstrated that intravenously injected nanoparticles targeting ICAM-1 specifically localized into the vasculature associated with the tumor progression. With further improvement of detection sensitivity in addition to more native tumor models containing not only tumor cells themselves but also fully-developed vasculatures and other stroma cells such as macrophages, our nanoparticles may provide a universal tumor imaging strategy not by tumor surface markers limited to specific cancer types but by the inflamed microenvironment which is associated with almost all cancer development.

Besides sensitive detection of chronic inflammation implicated in cancer, prompt and accurate detection of acute inflammation induced by bacterial or viral infection such as sepsis is also of clinical importance. Acute inflammation dramatically induces ICAM-1 induction not only in endothelium but also in immune cells, such that both cellular components become the targets by I domain-coated nanoparticle. Using LPS-induced acute inflammation model, we demonstrated optical imaging of the temporal dynamics of inflammation. Specific localization of LMN was also confirmed by QSM technique using MRI. The degree of localization of ICAM-1 targeting nanoparticles into an inflamed site will closely reflect different phases of inflammation, from the onset of inflammation to resolution phase. Therefore, quantitative prediction of spatiotemporal distribution of nanoparticles may provide critical information on diagnosis and the choice of therapy regimen in clinics.

In summary, our ICAM-1 targeting strategy by mimicking the behavior of leukocytes in their ability to localize to the inflamed endothelium was able to detect ICAM-1 overexpression in tumor cells, tumor vascular microenvironment, and acute inflammation. In the design of ICAM-1 targeting nanoparticles by conjugation with LFA-1 I domain, we employed His-tag binding to nickel-NTA, which we previously found [17] to be critical in order to fine-tune the coating density of targeting moieties to be specific to ICAM-1 overexpression but not to basally present ICAM-1. The idea of optimizing molecular interactions by tuning the avidity between ligands and receptors could provide a useful strategy to molecular targeting of some important targets that are basally expressed elsewhere. Inflammation-targeting nanoparticles with the lipid layer shell can also be used to carry small, hydrophobic drugs, achieving simultaneous imaging and targeted drug delivery.

5. Conclusion

This study presents physiology-inspired design of SPIO nanoparticles for *in vivo* detection by optical imaging and MRI, mimicking activated leukocyte in its ability to recognize inflamed endothelium. Nanoparticles *in vivo* will experience hydrodynamic force induced by the blood flow, requiring simultaneous molecular interactions with sufficient adhesion strength with the cells for nanoparticles to remain on cell surface. Therefore, the design of nanoparticles with tunable affinity and avidity of physiological interactions would be critical to selectivity and efficiency of leukocyte-mimetic nanoparticles in targeting inflammation. Notably, we observed specific accumulation of systemically-delivered nanoparticles into the vasculature within the tumor

and invasive tumor front where the tumor growth and angiogenesis were active, while their localization into the vasculature elsewhere was much lower. The use of two different nanoparticles differed only by the type of I domains (active vs. inactive) as targeting moieties against ICAM-1 enabled us to discriminate inflammation-driven accumulation into the tumor microenvironment from passive distribution, which may result from the leakiness of the vasculature within the tumor. Inflammation-targeting nanoparticles such as SPIO with the layer of phospholipid are also suitable for carrying small molecule drugs, achieving simultaneous imaging and targeted drug delivery.

References

[1] Nathan C, Ding A. Nonresolving inflammation. Cell 2010;140:871–82.
[2] Cohen J. The immunopathogenesis of sepsis. Nature 2002;420:885–91.
[3] Glass CK, Saijo K, Winner B, Marchetto MC, Gage FH. Mechanisms underlying inflammation in neurodegeneration. Cell 2010;140:918–34.
[4] Libby P. Inflammation in atherosclerosis. Nature 2002;420:868–74.
[5] Hotamisligil GS. Inflammation and metabolic disorders. Nature 2006;444: 860–7.
[6] Coussens LM, Werb Z. Inflammation and cancer. Nature 2002;420:860–7.
[7] Mantovani A, Allavena P, Sica A, Balkwill F. Cancer-related inflammation. Nature 2008;454:436–44.
[8] Sipkins DA, Gijbels K, Tropper FD, Bednarski M, Li KC, Steinman L. ICAM-1 expression in autoimmune encephalitis visualized using magnetic resonance imaging. J Neuroimmunol 2000;104:1–9.
[9] Weller GE, Lu E, Csikari MM, Klibanov AL, Fischer D, Wagner WR, et al. Ultrasound imaging of acute cardiac transplant rejection with microbubbles targeted to intercellular adhesion molecule-1. Circulation 2003;108:218–24.
[10] Zhang N, Chittasupho C, Duangrat C, Siahaan TJ, Berkland C. PLGA nanoparticle–peptide conjugate effectively targets intercellular cell-adhesion molecule-1. Bioconjug Chem 2008;19:145–52.
[11] Kelly KA, Allport JR, Tsourkas A, Shinde-Patil VR, Josephson L, Weissleder R. Detection of vascular adhesion molecule-1 expression using a novel multimodal nanoparticle. Circ Res 2005;96:327–36.
[12] Voinea M, Manduteanu I, Dragomir E, Capraru M, Simionescu M. Immunoliposomes directed toward VCAM-1 interact specifically with activated endothelial cells—a potential tool for specific drug delivery. Pharm Res 2005;22: 1906–17.
[13] Nahrendorf M, Keliher E, Panizzi P, Zhang H, Hembrador S, Figueiredo JL, et al. 18F-4V for PET-CT imaging of VCAM-1 expression in atherosclerosis. JACC Cardiovasc Imaging 2009;2:1213–22.
[14] Ehrhardt C, Kneuer C, Bakowsky U. Selectins-an emerging target for drug delivery. Adv Drug Deliv Rev 2004;56:527–49.
[15] Chan JM, Zhang L, Tong R, Ghosh D, Gao W, Liao G, et al. Spatiotemporal controlled delivery of nanoparticles to injured vasculature. Proc Natl Acad Sci U S A 2010;107:2213–8.
[16] Dustin ML, Rothlein R, Bhan AK, Dinarello CA, Springer TA. Induction by IL 1 and interferon-gamma: tissue distribution, biochemistry, and function of a natural adherence molecule (ICAM-1). J Immunol 1986;137:245–54.
[17] Kang S, Park T, Chen X, Dickens G, Lee B, Lu K, et al. Tunable physiologic interactions of adhesion molecules for inflamed cell-selective drug delivery. Biomaterials 2011;32:3487–98.
[18] Jin M, Song G, Carman CV, Kim YS, Astrof NS, Shimaoka M, et al. Directed evolution to probe protein allostery and integrin I domains of 200,000-fold higher affinity. Proc Natl Acad Sci U S A 2006;103:5758–63.
[19] Liu T, Spincemaille P, de Rochefort L, Kressler B, Wang Y. Calculation of susceptibility through multiple orientation sampling (COSMOS): a method for conditioning the inverse problem from measured magnetic field map to susceptibility source image in MRI. Magn Reson Med 2009;61:196–204.
[20] Wharton S, Schafer A, Bowtell R. Susceptibility mapping in the human brain using threshold-based k-space division. Magn Reson Med 2010;63: 1292–304.
[21] Weber C, Fraemohs L, Dejana E. The role of junctional adhesion molecules in vascular inflammation. Nat Rev Immunol 2007;7:467–77.
[22] Shimaoka M, Lu C, Palframan RT, von Andrian UH, McCormack A, Takagi J, et al. Reversibly locking a protein fold in an active conformation with a disulfide bond: integrin alphaL I domains with high affinity and antagonist activity in vivo. Proc Natl Acad Sci U S A 2001;98:6009–14.

[23] Marlin SD, Springer TA. Purified intercellular adhesion molecule-1 (ICAM-1) is a ligand for lymphocyte function-associated antigen 1 (LFA-1). Cell 1987;51: 813–9.

[24] Park S, Kang S, Veach AJ, Vedvyas Y, Zarnegar R, Kim JY, et al. Self-assembled nanoplatform for targeted delivery of chemotherapy agents via affinity-regulated molecular interactions. Biomaterials 2010;31:7766–75.

[25] Dubertret B, Skourides P, Norris DJ, Noireaux V, Brivanlou AH, Libchaber A. In vivo imaging of quantum dots encapsulated in phospholipid micelles. Science 2002;298:1759–62.

[26] Kelly CP, O'Keane JC, Orellana J, Schroy 3rd PC, Yang S, LaMont JT, et al. Human colon cancer cells express ICAM-1 in vivo and support LFA-1-dependent lymphocyte adhesion in vitro. Am J Phys 1992;263:G864–70.

[27] Maurer CA, Friess H, Kretschmann B, Wildi S, Muller C, Graber H, et al. Over-expression of ICAM-1, VCAM-1 and ELAM-1 might influence tumor progression in colorectal cancer. Int J Cancer 1998;79:76–81.

[28] Hayes SH, Seigel GM. Immunoreactivity of ICAM-1 in human tumors, metastases and normal tissues. Int J Clin Exp Pathol 2009;2:553–60.

[29] Reinhardt M, Hauff P, Linker RA, Briel A, Gold R, Rieckmann P, et al. Ultrasound derived imaging and quantification of cell adhesion molecules in experimental autoimmune encephalomyelitis (EAE) by Sensitive Particle Acoustic Quantification (SPAQ). Neuroimage 2005;27:267–78.

[30] Osborn L. Leukocyte adhesion to endothelium in inflammation. Cell 1990; 62:3–6.

[31] Springer TA. Adhesion receptors of the immune system. Nature 1990;346: 425–34.

[32] Shi W, Wang J, Fan X, Gao H. Size and shape effects on diffusion and absorption of colloidal particles near a partially absorbing sphere: implications for uptake of nanoparticles in animal cells. Phys Rev E Stat Nonlin Soft Matter Phys 2008;78. 061914.

[33] Mailander V, Landfester K. Interaction of nanoparticles with cells. Biomacromolecules 2009;10:2379–400.

[34] Rajashekhar G, Willuweit A, Patterson CE, Sun P, Hilbig A, Breier G, et al. Continuous endothelial cell activation increases angiogenesis: evidence for the direct role of endothelium linking angiogenesis and inflammation. J Vasc Res 2006;43:193–204.

[35] Franses JW, Baker AB, Chitalia VC, Edelman ER. Stromal endothelial cells directly influence cancer progression. Sci Transl Med 2011;3. 66ra5.

[36] Pandolfi F, Trentin L, Boyle LA, Stamenkovic I, Byers HR, Colvin RB, et al. Expression of cell adhesion molecules in human melanoma cell lines and their role in cytotoxicity mediated by tumor-infiltrating lymphocytes. Cancer 1992; 69:1165–73.

[37] Kobayashi H, Boelte KC, Lin PC. Endothelial cell adhesion molecules and cancer progression. Curr Med Chem 2007;14:377–86.

[38] Nelson H, Ramsey PS, Donohue JH, Wold LE. Cell adhesion molecule expression within the microvasculature of human colorectal malignancies. Clin Immunol Immunopathol 1994;72:129–36.

[39] Fox SB, Turner GD, Leek RD, Whitehouse RM, Gatter KC, Harris AL. The prognostic value of quantitative angiogenesis in breast cancer and role of adhesion molecule expression in tumor endothelium. Breast Cancer Res Treat 1995;36:219–26.

[40] Suzuki Y, Ohtani H, Mizoi T, Takeha S, Shiiba K, Matsuno S, et al. Cell adhesion molecule expression by vascular endothelial cells as an immune/inflammatory reaction in human colon carcinoma. Jpn J Cancer Res 1995;86: 585–93.

[41] Cianchi F, Cuzzocrea S, Vinci MC, Messerini L, Comin CE, Navarra G, et al. Heterogeneous expression of cyclooxygenase-2 and inducible nitric oxide synthase within colorectal tumors: correlation with tumor angiogenesis. Dig Liver Dis 2010;42:20–7.